Article

Midlatitude mesoscale thermal Air-sea interaction enhanced by greenhouse warming

Check for updates

Xiaohui Ma [1,2], Xingzhi Zhang [2] ✉, Lixin Wu [1,2], Zhili Tang[1], Peiran Yang[2], Fengfei Song [1,2], Zhao Jing [1,2], Hui Chen[1], Yushan Qu[1], Man Yuan[1], Zhaohui Chen [1,2] & Bolan Gan [1,2]

The influence of greenhouse warming on mesoscale air-sea interactions, crucial for modulating ocean circulation and climate variability, remains largely unexplored due to the limited resolution of current climate models. Additionally, there is a lack of theoretical frameworks for assessing changes in mesoscale coupling due to warming. Here, we address these gaps by analyzing eddy-resolving high-resolution climate simulations and observations, focusing on the mesoscale thermal interaction dominated by mesoscale sea surface temperature (SST) and latent heat flux (LHF) coupling in winter. Our findings reveal a consistent increase in mesoscale SST-LHF coupling in the major western boundary current regions under warming, characterized by a heightened nonlinearity between warm and cold eddies and a more pronounced enhancement in the northern hemisphere. To understand the dynamics, we develop a theoretical framework that links mesoscale thermal coupling changes to large-scale factors, which indicates that the projected changes are collectively determined by historical background wind, SST, and the rate of SST warming. Among these factors, the large-scale SST and its warming rate are the primary drivers of hemispheric asymmetry in mesoscale coupling intensification. This study introduces a simplified approach for assessing the projected mesoscale thermal coupling changes in a warming world.

Mesoscale air-sea interactions, predominantly active in the Western Boundary Current (WBC) regions in the midlatitudes, play a critical role in modulating extratropical weather and climate systems[1–5]. The interaction between mesoscale oceanic eddies and the atmosphere actively impacts precipitation, storms, large-scale atmospheric circulations, and provides feedback to the ocean, influencing oceanic circulations and climate variability[6–15]. A key aspect of this interaction is the coupling between sea surface temperature and turbulent heat flux (SST-THF), hereafter denoted as thermal coupling. In terms of the atmosphere, thermal coupling acts as an energy source, which is crucial for the genesis and development of weather systems and deep

troposphere response[16–21]. In terms of the ocean, thermal coupling serves as an energy sink, which is the key to dissipating oceanic eddy energy and driving oceanic circulation response[11,22].

How greenhouse warming will impact mesoscale oceanic eddies remains uncertain, let alone mesoscale air-sea coupling. Satellite observations reveal a rise in eddy activity in the WBC regions during recent decades, while climate models project heterogeneous eddy variations in different WBC regions under warming[23,24]. Additionally, the theoretical framework for predicting the mesoscale thermal coupling change in response to greenhouse warming is currently absent. Thermodynamically, the SST warming and the associated water vapor

[1]Frontiers Science Center for Deep Ocean Multispheres and Earth System and Key Laboratory of Physical Oceanography, Ocean University of China, Qingdao, China. [2]Laoshan Laboratory, Qingdao, China. ✉e-mail: zhangxingzhi@ouc.edu.cn

increase governed by the Clausius–Clapeyron (C-C) relation, appear to strengthen the thermal air-sea coupling (primarily through the enhancement of latent heat flux) in a warming climate. Dynamically, the non-uniform warming between the upper and lower troposphere under anthropogenic forcing tends to increase atmospheric stability, inhibiting the vertical momentum transfer and thereby suppressing the surface wind and thermal air-sea coupling. This is further complicated by significant uncertainties in atmospheric circulation responses under climate change, introducing additional perturbations to SST-THF coupling. It is noteworthy that the aforementioned oceanic and atmospheric changes discussed within a conventional large-scale framework may not necessarily manifest at mesoscales. Physical processes governing the response of mesoscale thermal coupling to greenhouse warming are multifaceted, making it challenging to pinpoint the ultimate dominant factor.

Utilizing an unprecedented set of high-resolution Community Earth System Model (referred to as CESM-HR, Methods) with ~0.25° atmosphere and ~0.1° ocean components that can explicitly resolve the mesoscale oceanic eddies and their coupling with the atmosphere, we investigated the impact of greenhouse warming on mesoscale thermal coupling in eddy-rich WBC regions. We then constructed a theoretical framework for estimating the mesoscale thermal coupling change in response to greenhouse warming through the decomposition of contributing factors. We further assessed the robustness of the findings by extending the analyses to High-Resolution Model Intercomparison Project (HighResMIP, Methods) models.

Results

Mesoscale thermal coupling during the observational period

We first evaluated the model's capability in representing the mesoscale thermal coupling in the CESM-HR simulations against observational data (Methods), in four major WBC regions, i.e., the Kuroshio Extension (KE), the Gulf Stream Extension (GS), the Agulhas Return Current (ARC) and the Brazil-Malvinas Confluence Region (BMC), by detecting eddies using sea surface height anomalies and constructing composite analyses with a reference frame centered on the eddy (see details in Methods). The model shows high fidelity in representing the statistical characteristics of eddies, such as the averaged number, amplitude and size, as detailed in Tab. S1. It also successfully reproduces the eddy-induced turbulent heat fluxes (including both sensible and latent components) along with their seasonality, for both anticyclonic warm and cyclonic cold eddies (Fig. S1). It is noted that the coupling strength peaks during the winter month. Furthermore, the eddy-induced sensible heat flux (SHF) is approximately half that of latent heat flux (LHF) and the differences between historical and future simulations are subtle (Fig. S2). Thus, the mesoscale thermal coupling in the WBC regions and its response to global warming is predominantly influenced by LHF. Consequently, our subsequent analyses will focus on the mesoscale SST-LHF coupling in the hemispheric winter season – DJF for the Northern Hemisphere (NH) and JJA for the Southern Hemisphere (SH).

To assess the potential impact of anthropogenic warming on mesoscale thermal coupling, we analyzed the decadal trend of mesoscale SST-LHF coupling in the observational periods based on high-pass spatial filtering fields (Methods). A significant intensification of mesoscale SST-LHF coupling at an approximate rate of 1.5 W/m²/°C per decade is detected in the WBCs over the past four decades, with the most pronounced increase observed in the GS and KE regions of the NH (Fig. 1a). The CESM-HR successfully simulates the enhanced mesoscale thermal coupling in the WBCs with a magnitude slightly higher than that recorded in the observations (Fig. 1b). The model also captures the north-south hemispheric asymmetry of the changes. The alignment between model simulated and observational trends in the past lends credence to the use of CESM-HR for investigating the mesoscale coupling response under climate change.

Mesoscale thermal coupling under greenhouse warming

A linear regression between mesoscale SST and LHF based on eddy composites averaged across four WBC regions, yields an estimated coupling coefficient of approximately 29 W/m²/°C for both anticyclonic warm and cyclonic cold eddies in historical simulations (1956–2005, Fig. 1c, d). The nonlinearity between warm and cold eddies appears to be minimal during the historical period. Under the high greenhouse forcing scenario of Representative Concentration Pathway 8.5, future simulations (2063-2100) project an approximate 14% enhancement in mesoscale SST-LHF coupling to 33 W/m²/°C (Fig. 1d). A detailed examination of the four WBCs reveals a consistent increase in coupling strength by 6% to 18% in future simulations compared to historical simulations (Fig. 1e). Importantly, future simulations project a greater increase of mesoscale SST-LHF coupling strength for warm eddies than for cold eddies, indicating heightened nonlinearity in a warming climate. The increase in nonlinearity is expected to amplify net heat flux from mesoscale oceanic eddies[13,25], thereby impacting future weather and climate systems more significantly. Additionally, the projected increase in mesoscale SST-LHF coupling in the GS and KE is nearly twice that of the ARC and BMC, pointing to a more substantial intensification in the NH than in the SH. Combined with the findings in the observational periods, the results indicate that the hemisphere discrepancy in mesoscale SST-LHF coupling is likely to not only persist but also to become more pronounced with ongoing climate warming.

Decomposition of contributing factors

The LHF is proportional to both the surface wind and the humidity difference at the air-sea interface according to the Bulk formula[26]. To estimate the mesoscale SST-LHF coupling associated with oceanic eddies, we decompose the relevant fields into large-scale background and mesoscale components in line with previous studies[27,28]. The mesoscale SST-LHF coupling coefficient can be quantified using the following relationship (see detailed derivation in Methods):

$$\frac{dQ_L'}{dSST'} = \bar{\rho}_a \bar{\Lambda}_v \bar{C}_e \left[\bar{U}_{10} \left(\frac{dq_s'}{dSST'} - \frac{dq_a'}{dSST'} \right) + \frac{dU_{10}'}{dSST'} (\bar{q}_S - \bar{q}_a) \right] \quad (1)$$

Here, the prime (′) represents mesoscale anomalies defined by the high-pass spatial filtering, and the overbar (¯) denotes large-scale background excluding the mesoscale signal.

The mesoscale SST-LHF coupling coefficient $\left(\frac{dQ_L'}{dSST'} \right)$ is determined by two components: the thermodynamic adjustment to mesoscale SST multiplied by the largescale wind ($\bar{U}_{10} \left(\frac{dq_s'}{dSST'} - \frac{dq_a'}{dSST'} \right)$, hereafter denoted as mesoscale thermodynamic adjustment term), and the dynamic adjustment to mesoscale SST multiplied by the large-scale humidity difference ($\frac{dU_{10}'}{dSST'} (\bar{q}_S - \bar{q}_a)$, hereafter denoted as mesoscale dynamic adjustment term). Evaluation of historical and future simulations in the WBC regions reveals an increase in both terms due to greenhouse forcing (bars with black borders in Fig. 2a–d). Particularly, the enhancement of the thermodynamic adjustment term is about 3 to 5 times that of the dynamic adjustment term across all four WBCs (Fig. 2a–d), indicating the dominant contribution of the thermodynamic adjustment term to mesoscale SST-LHF coupling modulation.

Although the dynamic adjustment term is substantially weaker than the thermodynamic adjustment, it is notably stronger in the NH compared to the SH. A decomposition of the dynamic adjustment term shows that the response of large-scale air-sea humidity difference under warming generally surpasses the mesoscale wind response to oceanic eddies across the four WBCs (Fig. S3). However, the mesoscale wind response to eddies is more pronounced in the KE and GS regions and minimal in the ARC and BMC regions, contributing to the stronger mesoscale dynamic adjustment in the NH. The intensified mesoscale wind response to eddies in the KE and GS may be associated with the

vigorous western boundary currents, stronger oceanic eddy activities[8], and the frequent passage of synoptic weather systems that collocate with the KE and GS. These factors lead to an unstable planetary boundary layer and enhanced downward momentum transfer as discussed in previous studies[2,29].

A further decomposition of the thermodynamic adjustment term reveals that the large-scale wind change between historical and future simulations is negligible (bars with magenta borders in Fig. 2a–d), while the predominant influence arises from the mesoscale moisture response to oceanic eddies, especially the specific humidity change at the ocean surface. Specifically, $\frac{dq'_s}{dSST'}$ is an order of magnitude greater than $\frac{dq'_a}{dSST'}$, which may be attributed to the atmospheric boundary layer thermal adjustment that results in a reduced surface air temperature anomaly relative to the mesoscale SST anomaly as indicated by Moreton et al. (2021)[30] and Hausmann et al.[31]. Collectively, the results suggest that the amplification in mesoscale moisture response is the principal driver for the strengthened mesoscale SST-LHF coupling under climate change.

The above analyses indicate that changes in mesoscale SST-LHF coupling due to warming can be effectively estimated via the mesoscale moisture adjustment process. Nonetheless, this estimation still relies on the availability of both mesoscale and large-scale fields from historical and future simulations. To circumvent this, we apply a Taylor series expansion to the mesoscale moisture derivative (see detailed derivation in Methods). The resultant expression provides a simplified approach to assess mesoscale SST-LHF coupling change using large-scale fields:

$$\left(\frac{dQ'_L}{dSST'}\right)_{(F-P)} = \left(\bar{\rho}_a \bar{\Lambda}_v \bar{C}_e\right)_{(P)} \cdot \bar{U}_{10(P)} \left(\frac{d^2 q_s(T)}{dT^2}\Big|_{T=\overline{SST}_{(P)}} \cdot \Delta\overline{SST}\right) \quad (2)$$

Here, 'F' represents future values and 'P' represents historical values in the past. It is evident that changes in mesoscale SST-LHF coupling are collectively affected by the large-scale wind and the curvature of the C-C scaling from the historical simulations, along with the projected warming of large-scale SST. Note that the curvature of the C-C scaling is inherently linked with the background SST, with higher temperature corresponding to a more pronounced moisture-temperature sensitivity. The relationship suggests that projections of future mesoscale SST-LHF coupling are significantly influenced by the historical large-scale oceanic and atmospheric conditions. Given that the large-scale wind and the
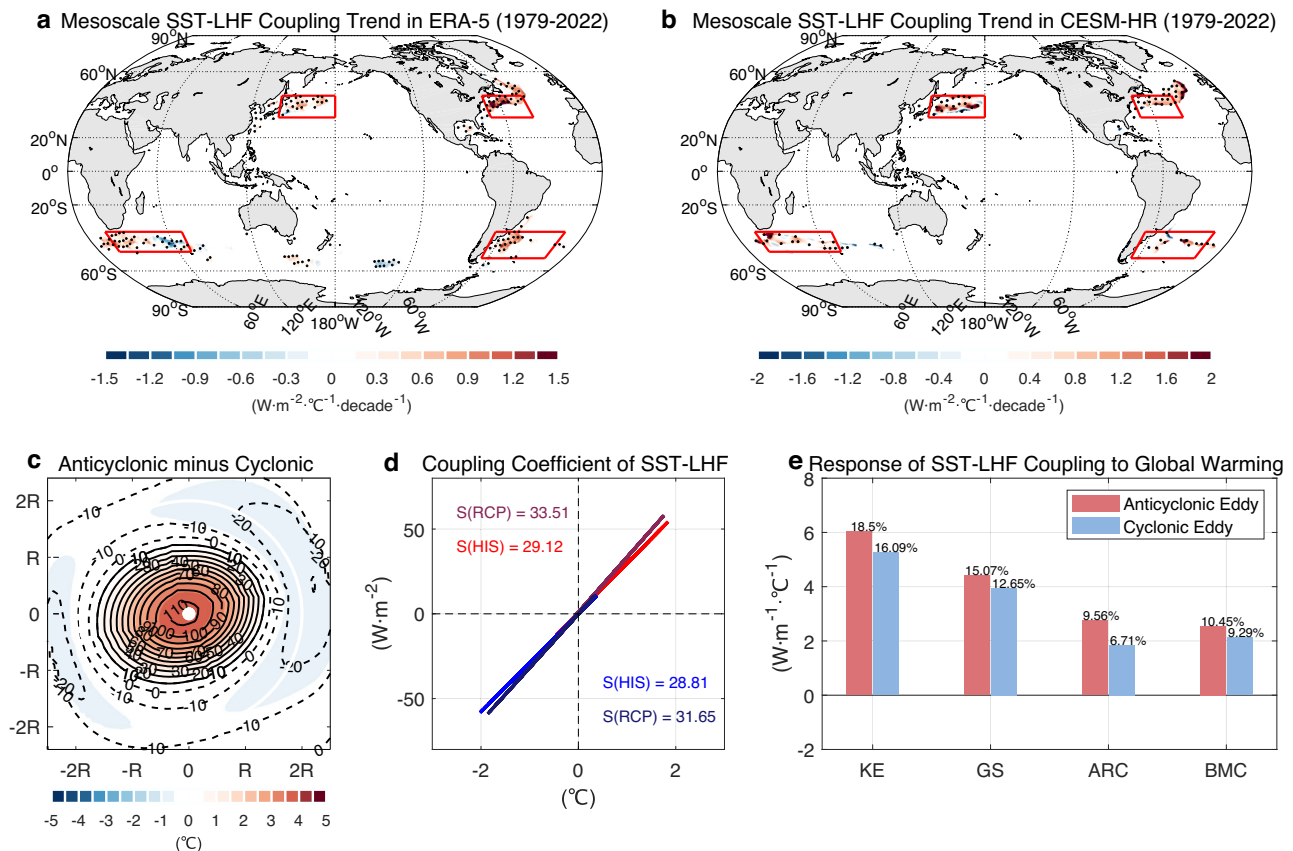

Fig. 1 | Observed and simulated trends in mesoscale sea surface temperature-latent heat flux (SST-LHF) coupling. Global distribution of the decadal trends of mesoscale SST-LHF coupling strength as derived from the fifth generation European Centre for Medium-Range Weather Forecasts atmospheric reanalysis (ERA5) (**a**) and high-resolution Community Earth System Model (CESM-HR) (**b**) during 1979–2022. The coupling strength is computed using the linear regression coefficient between high-pass filtered monthly SST and LHF (Methods) with trends significant at a 99% confidence level indicated by black dots. **c** Composites of SST (color shading, °C) and LHF (contours, W/m²) anomalies associated with mesoscale oceanic eddies during historical periods (1956-2005) in CESM-HR. Shown are winter season mean anomalies in anticyclonic warm minus cyclonic cold eddy composites within four western boundary current (WBC) regions (outlined by red boxes in **a**, **b**).

The white circle represents one eddy radius and the white dot marks the eddy center. **d** Mesoscale SST-LHF coupling strength (W/m²/°C) during historical (HIS, 1956–2005) and future (RCP, 2063-2100) periods in CESM-HR for warm (red) and cold (blue) eddies averaged across four WBC regions. The coupling strength is computed using the linear regression coefficient between SST and LHF anomalies within twice the radius of eddy composites. **e** Differences in mesoscale SST-LHF coupling strength between future and historical periods in CESM-HR for warm (red bars) and cold (blue bars) eddies in the Kuroshio Extension (KE), the Gulf Stream (GS), the Agulhas Return Current (ARC) and the Brazil-Malvinas Confluence Region (BMC) regions, with fractional differences labeled atop the respective bars. Source data are provided as a Source Data file.
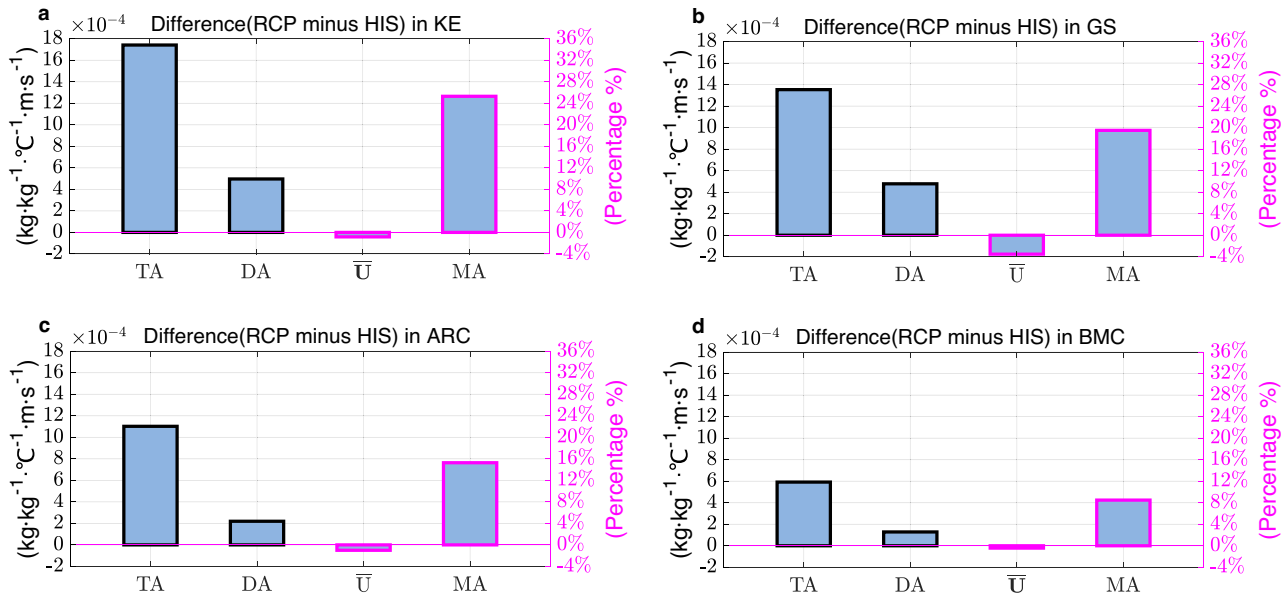
Fig. 2 | Decomposition of mesoscale sea surface temperature-latent heat flux (SST-LHF) coupling response under greenhouse warming. a Differences in thermodynamic and dynamic adjustments between future (RCP) and historical (HIS) periods in high-resolution Community Earth System Model (CESM-HR) in the Kuroshio Extension (KE) region. From left to right, the terms plotted are thermodynamic adjustment (TA), $\bar{U}_{10}\left(\frac{dq'_s}{dSST'} - \frac{dq'_a}{dSST'}\right)$, dynamic adjustment (DA), $\frac{dU'_{10}}{dSST'}(\bar{q}_S - \bar{q}_a)$, large-scale surface wind ($\bar{U}_{10}$) and moisture adjustment (MA), $\left(\frac{dq'_s}{dSST'} - \frac{dq'_a}{dSST'}\right)$. (**b**–**d**), as for (**a**), but for the Gulf Stream (GS), the Agulhas Return Current (ARC) and the Brazil-Malvinas Confluence Region (BMC) regions, respectively. Source data are provided as a Source Data file.

curvature of the C-C scaling stay positive, it can be inferred that the direction of mesoscale SST-LHF coupling is exclusively determined by the sign of projected SST changes, leading to consistent intensification in line with the warming of underlying SST.

We then assessed the regional variations in mesoscale SST-LHF coupling responses among the four WBC regions using Eq. (2), with emphasis on the north-south hemisphere asymmetry. The simplified relationship efficiently captures the more pronounced increase in coupling strength within the KE and GS regions compared to the ARC and BMC regions (Fig. 3a), consistent with the projected intensification of mesoscale SST-LHF coupling between future and historical simulations. Detailed examination of contributing factors in CESM-HR demonstrates consistently higher values for large-scale wind and SST in the KE and GS regions in the NH from historical simulations, alongside a more rapid SST warming rate (Fig. 3c), all of which jointly contribute to the enhanced augmentation in mesoscale coupling strength in the NH under climate change. The historical large-scale wind in the KE is approximately 30% stronger than that in the ARC and BMC, and the background SST in the GS is 7 °C higher than in the BMC, corroborated by observations (Fig. 3d). Additionally, the accelerated SST warming trend in the NH than in the SH is also confirmed by the observational data (Fig. 3d), underscoring the robustness of the hemisphere asymmetry under warming. Further decomposition of the three factors indicates their respective contribution to the overall hemispheric discrepancy (Fig. 3b), with the large-scale SST warming rate being the dominant factor, followed by the background SST.

Validations in HighResMIP

We extend the analyses to HighResMIP simulations (Methods) and to different warming periods (2030–2050), aiming to verify the robustness of the findings. All models examined show an increase in mesoscale SST-LHF coupling in response to greenhouse warming across four WBCs by the year 2050 (Tab. 1). A more pronounced intensification of this coupling is projected in the NH compared to the SH, in line with CESM-HR results (Fig. 1e), albeit with a generally lower magnitude of change. The magnitude discrepancy is due to the

HighResMIP projections here terminating in 2050, whereas CESM-HR projections shown in Fig. 1 extend to a later period of the century (2100).

The effectiveness of the proposed theoretical framework for estimating changes in mesoscale SST-LHF coupling due to greenhouse warming was also evaluated across different models. A comparison between the coupling strength changes estimated by the theoretical framework and those projected by CESM-HR reveals a significant linear relationship across four WBCs (Fig. S4). The estimated and actual projected changes in mesoscale SST-LHF coupling are highly correlated, with a correlation coefficient of around 0.7 in the KE and GS, and 0.5 in the ARC and BMC (Tab. 1). Similar linear correlations, ranging generally from 0.5 to 0.8 (Tab. 1), are found between estimated and projected mesoscale coupling strength changes in HighResMIP models, confirming the broad applicability of the simplified framework across diverse climate models.

Discussion

How greenhouse warming will influence mesoscale air-sea interactions remains an open question. Utilizing eddy-resolving high-resolution CESM simulations, supported by observational and HighResMIP data, we found a ubiquitous intensification of mesoscale thermal coupling in WBC regions by the end of the 21st century under the RCP8.5 warming scenario. The intensification is primarily driven by mesoscale SST-LHF coupling and is characterized by an increased nonlinearity between warm and cold eddies and a more pronounced enhancement in the NH. Considering the recognized importance of mesoscale oceanic processes in influencing weather and climate systems, as highlighted in previous studies[4,5,11], our results underscore the critical need for climate models to incorporate mesoscale air-sea interaction for more reliable climate projections.

We found that the mesoscale moisture response is the key factor driving the strengthened mesoscale SST-LHF coupling under climate change. To further understand the dynamics, we developed a theoretical framework to estimate the mesoscale moisture change. The framework builds a linkage between mesoscale coupling changes and
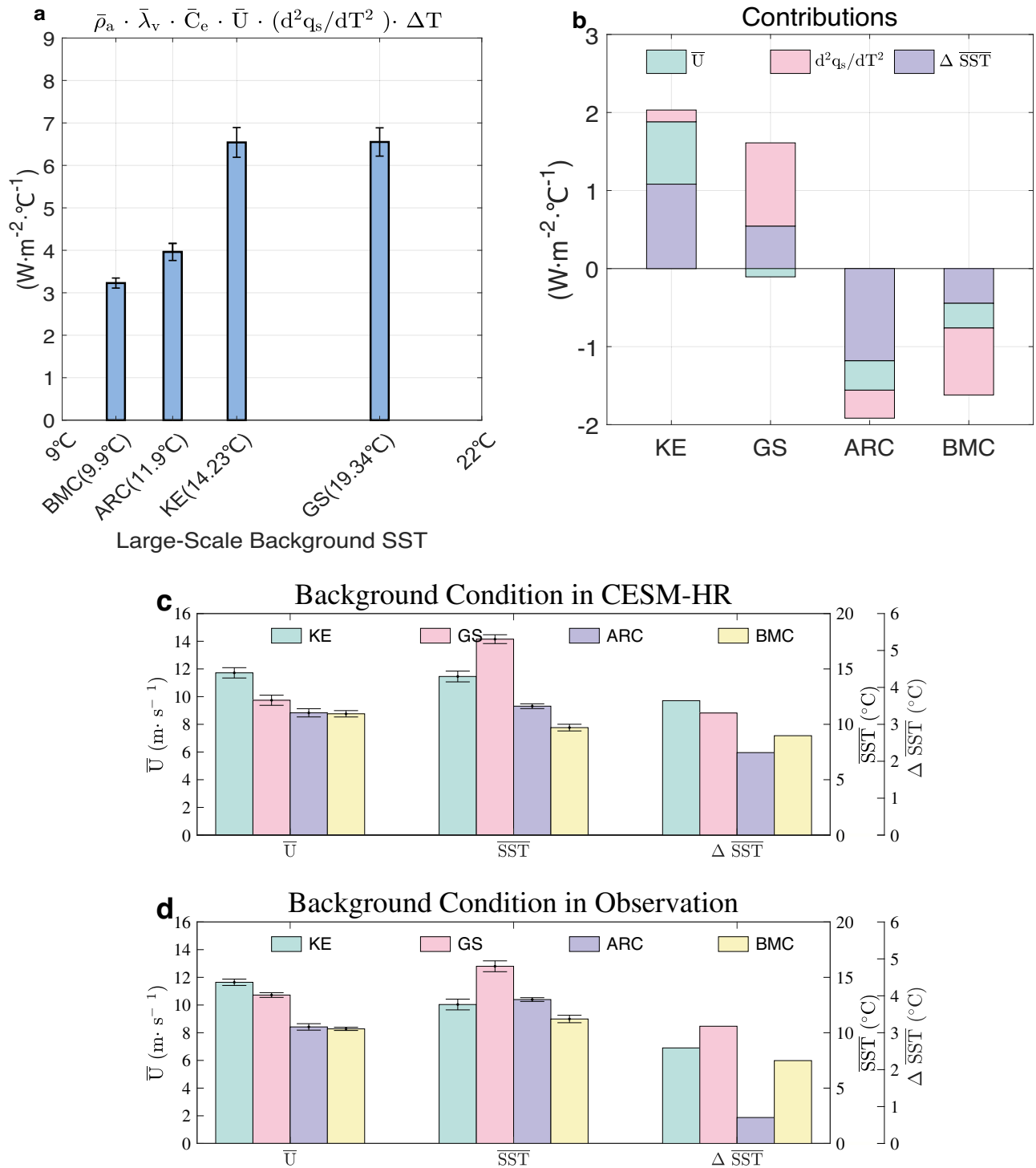
Fig. 3 | Decomposition of mesoscale moisture response under greenhouse warming. a Estimated changes in mesoscale sea surface temperature-latent heat flux (SST-LHF) coupling between future and historical periods in high-resolution Community Earth System Model (CESM-HR) according to Eq. (2) in the Kuroshio Extension (KE), the Gulf Stream (GS), the Agulhas Return Current (ARC) and the Brazil-Malvinas Confluence Region (BMC) regions. The large-scale SST averaged in the western boundary current (WBC) is displayed on the bottom axis for each respective region. **b** Contributions of $\bar{U}_{10}$ (A), $\frac{d^2 q_s(T)}{dT^2}$ (B) and $\Delta \overline{SST}$ (C) to regional variations in mesoscale SST-LHF coupling response to global warming in the four WBCs. Taking the KE region as an example, the deviation of $\frac{dQ'_l}{dSST}$ response from the four-WBC mean can be represented as: $\left(\frac{dQ'_l}{dSST}\right)|_{(KE-WBCmean)} = A'\bar{B}\bar{C} + B'\bar{A}\bar{C} + C'\bar{A}\bar{B}$. Here, A, B, and C denotes the respective three terms; the overbar denotes the

average values across the four WBCs; the prime denotes the deviation from the WBC mean. For instance, $A'\bar{B}\bar{C}$ calculates the $A'(\bar{U}_{10}$ anomaly) contribution to the total anomaly, assuming that B and C are at their mean levels, as represented by the green bar in (**b**). **c** The historical large-scale surface wind, SST and the projected SST warming (future minus historical periods) within the four WBC regions in CESM-HR. (**d**) as for (**c**), but for observational data. Surface wind is derived from the fifth generation European Centre for Medium-Range Weather Forecasts atmospheric reanalysis (ERA5) and SST is derived from the National Oceanic and Atmospheric Administration daily Optimum Interpolation SST (NOAA-OISST). $\Delta \overline{SST}$ (°C per century) is computed based on the warming trend observed over the last 40 years. The error bars in a,c and d represent the interannual standard deviation of corresponding variables for each region. Source data are provided as a Source Data file.

Table. 1 | Projected and estimated mesoscale sea surface temperature-latent heat flux (SST-LHF) coupling changes in high-resolution Community Earth System Model (CESM-HR) and High-Resolution Model Intercomparison Project (HighResMIP) models in four major western boundary current regions, i.e., the Kuroshio Extension (KE), the Gulf Stream (GS), the Agulhas Return Current (ARC) and the Brazil-Malvinas Confluence Region (BMC). Source data are provided as a Source Data file

	Projected coupling changes (RCP-HIS) ($W \cdot m^{-2} \cdot {}^{\circ}C^{-1}$)				Correlation between projected and estimated changes			
	KE	GS	ARC	BMC	KE	GS	ARC	BMC
CESM-HR	3.2 (10.26%)	3.5 (15.34%)	1.9 (6.68%)	1.5 (6.72%)	0.71	0.69	0.45	0.49
CMCC-CM2-VHR4	4.1 (14.27%)	2.5 (11.97%)	1.5 (6.65%)	0.07 (0.35%)	0.76	0.65	0.60	0.54
HadGEM3-GC31-HH	3.2 (11.95%)	2.0 (8.76%)	2.8 (11.34%)	2.4 (11.88%)	0.78	0.66	0.58	0.61
MPI-ESM1-2-XR	2.9 (14.06%)	2.0 (10.14%)	1.6 (9%)	0.9 (5.24%)	0.41	0.69	0.72	0.78
EC-Earth3P-HR	2.0 (8.37%)	2.4 (11.24%)	1.5 (6.41%)	0.5 (2.72%)	0.72	0.76	0.69	0.66
CNRM-CM6-1-HR	2.2 (10.1%)	2.4 (12.4%)	1.2 (7.52%)	0.9 (3.58%)	0.69	0.7	0.67	0.58

Note that mesoscale SST-LHF coupling strength changes analyzed here correspond to differences between the historical period of 1950–1969 and the mid-21st century projections for the period of 2031–2050.

large-scale fields, revealing that the projected mesoscale moisture changes can be estimated by the interplay among historical background wind, SST, and projected SST warming. The direction of mesoscale SST-LHF coupling changes is exclusively determined by the sign of projected SST changes. Given a scenario of SST warming, the mesoscale SST-LHF coupling will invariably exhibit intensification. The relationship highlights the importance of C-C scaling in determining changes in mesoscale SST-LHF coupling, suggesting that higher large-scale SST, determined either by historical baselines or future warming rates, are associated with greater rates of moisture increase and thereby enhanced augmentation of mesoscale SST-LHF coupling.

The effectiveness of the proposed theoretical framework was evaluated across CESM-HR and HighResMIP models. The analysis reveals a robust linear correlation between estimated and projected changes in mesoscale SST-LHF, suggesting the broad applicability of the theoretical framework within major WBC regions. However, it is important to acknowledge that the prerequisite conditions for the theoretical framework to work are the mesoscale moisture adjustment significantly surpasses the mesoscale wind adjustment, the mesoscale moisture adjustment at the ocean surface significantly exceeds that at the atmospheric surface, and the large-scale wind changes due to warming is minimal. These conditions may not hold outside the WBCs, potentially undermining the framework's applicability.

It is important to recognize that an increase in mesoscale thermal coupling strength does not necessarily correspond to higher heat fluxes. The eddy composite analysis reveals a general increase in LHF across the WBCs, yet the accompanying eddies and SST anomalies are weakening (Fig. S5). This reduced eddy activity is possibly linked to enhanced mesoscale thermal coupling, which dampens eddy potential energy[11], and to increased oceanic stratification, which inhibits eddy formation. Further in-depth investigation is required to fully understand the changes in eddy dynamics under global warming.

Methods
CESM-HR, HighResMIP simulations and observations
We utilized the high-resolution Community Earth System Model (CESM-HR) simulations with ~0.25° atmosphere and ~0.1° ocean components developed by the National Center for Atmosphere Research (NCAR)[32]. The simulations include a 500-year preindustrial control simulation and a 250-year historical and future simulation from 1850 to 2100. Historical radiative forcing is applied from 1850 to 2005 while the Representative Concentration Pathway 8.5 (RCP8.5, a high greenhouse gas emission) warming forcing is switched from 2006 onwards. The longest available periods with high-frequency (daily) output were chosen to assess the mesoscale thermal coupling response to greenhouse warming in CESM-HR: a historical period from 1956 to 2005

(referred to as HIS) and a future period from 2063 to 2100 (referred to as RCP).

Five HighResMIP simulations with relatively high oceanic resolution were selected: CMCC-CM2-VHR4 (0.25° atmosphere and 0.25° ocean), HadGEM3-GC31-HH (0.5° atmosphere and 0.08° ocean), EC-Earth3P-HR (0.5° atmosphere and 0.25° ocean), CNRM-CM6-1-HR (1° atmosphere and 0.25° ocean), MPI-ESM1-2-XR (0.5° atmosphere and 0.5° ocean). We note that only one model (HadGEM3-GC31-HH) has comparable oceanic resolutions with CESM-HR, yet its atmospheric resolution is coarser. All these selected models include a 100-year historical and future (under RCP8.5 scenario) simulation from 1950 to 2050. For a consistent comparison between CESM-HR and HighResMIP simulations, 1950-1969 for historical and 2031-2050 for future projections were selected for the corroborative analysis shown in Table 1.

Daily sea surface height (SSH) derived from Copernicus Marine Environment Monitoring Service (CMEMS) during 2003–2007 was used to identify eddies in observations (Tab. S1). Concurrently, SST obtained from the National Oceanic and Atmospheric Administration daily Optimum Interpolation SST (NOAA-OISST) and heat fluxes derived from Japanese Ocean Flux Data Sets with Use of Remote Sensing Observations version3 (J-OFURO3) during the same period were employed to construct observational eddy composites (Fig. S1). ERA5 reanalysis (the fifth generation European Centre for Medium-Range Weather Forecasts atmospheric reanalysis[33]) with an extended temporal span from 1979 to 2022 was utilized to examine the decadal trend of mesoscale coupling strength (Fig. 1a).

Eddy detection, Eddy composites and high-pass filtering
In both CMEMS observations and CESM-HR simulations, mesoscale eddies were detected using daily SSH anomalies derived by applying high-pass spatial filtering (20° longitude x 10° latitude) to remove the large-scale signal, following previous studies[34,35]. Cyclonic (anticyclonic) eddies are classified by closed contours of SSH anomalies that include a single minimum (maximum), with an SSH anomaly increment (decrement) of 0.05 cm between successive contours. The edge of an eddy is delineated by the outmost closed contour of SSH anomalies. The radius of an eddy corresponds to the radius of a circle with an equivalent area to that enclosed by the outmost contour. The amplitude of an eddy is defined by the SSH anomaly difference between the eddy's peak and its defined edge. Only eddies with a radius ranging from 70 to 200 km and an amplitude exceeding 3 cm are included in the analysis.

Eddy composites were constructed by aligning associated variables to the reference coordinate of the eddy core. The variables were normalized by the individual eddy radius and oriented to the prevailing direction of the large-scale background surface wind, in line with

previous research[9]. Variables within twice the eddy radius were included for composite analysis.

In addition to eddy composite analysis, we also applied a high-pass Loess Filter with a cutoff wavelength of 30° longitude x 10° latitude (similar to a 5° x 5° box car average[3,11]) in ERA5, CESM-HR and HighResMIP, to isolate mesoscale SST and LHF and examined the spatial distribution of their coupling strength (Fig. 1a, b and Fig S4). The coupling strength at each grid point was computed using the linear regression coefficient between high-pass filtered monthly SST and LHF over a spatial domain of 4° x 4°. It was noted that applying a high-pass filter directly to monthly data yields a coupling coefficient comparable to that obtained when the filter is first applied to daily data, which is then aggregated into a monthly mean before calculating the coefficient. The former method was selected for its computational efficiency. To highlight regions with pronounced mesoscale SST-LHF coupling, mesoscale signals where the SST anomaly fell below 0.4 °C in ERA5, below 0.6 °C in CESM-HR, and coupling strength below 20 W/m²/°C in CESM-HR were excluded when computing the decadal trend in coupling strength (Fig. 1a, b).

Decomposition of mesoscale SST-LHF coupling

According to Bulk formula[26], the latent heat flux Q_L is determined by the equation:

$$Q_L = \rho_a \Lambda_v C_e U_{10}(q_s - q_a) \tag{3}$$

Here, ρ_a is the surface air density, Λ_v is the latent heat of vaporization, and C_e is the transfer coefficients for evaporation. U_{10} is the 10 m wind speed, q_s is the saturated specific humidity at the ocean surface, and q_a is air specific humidity at 2 m.

Following previous studies[27,28], Eq. (3) can be decomposed into large-scale background and mesoscale components. The mesoscale component of latent heat flux is estimated as follows:

$$Q_L' = \bar{\rho}_a \bar{\Lambda}_v \bar{C}_e [\bar{U}_{10}(q_s' - q_a') + U_{10}'(\bar{q}_S - \bar{q}_a)] \tag{4}$$

Here, the prime (′) represents mesoscale anomalies defined by the high-pass spatial filtering, and the overbar (̄) denotes large-scale background excluding the mesoscale signal.

By differentiating with respect to SST, the mesoscale SST-LHF coupling is expressed as:

$$\frac{dQ_L'}{dSST'} = \bar{\rho}_a \bar{\Lambda}_v \bar{C}_e \left[\bar{U}_{10} \left(\frac{dq_s'}{dSST'} - \frac{dq_a'}{dSST'} \right) + \frac{dU_{10}'}{dSST'} (\bar{q}_S - \bar{q}_a) \right] \tag{5}$$

Based on calculations, the second term $\frac{dU_{10}'}{dSST'}(\bar{q}_S - \bar{q}_a)$ on the right-hand side of Eq. (5) is an order of magnitude smaller than the first term $\bar{U}_{10}\left(\frac{dq_s'}{dSST'} - \frac{dq_a'}{dSST'}\right)$. Furthermore, $\frac{dq_a'}{dSST'}$ is an order of magnitude smaller than $\frac{dq_s'}{dSST'}$. Disregarding the relatively smaller terms and assuming the changes in $\bar{\rho}_a \bar{\Lambda}_v \bar{C}_e$ is minimal under global warming (with a relative change of approximately 2%, which is negligible compared to the 17% mesoscale moisture adjustment), the mesoscale SST-LHF coupling changes is predominately influenced by $\bar{U}_{10}\frac{dq_s'}{dSST'}$, which can be represented as:

$$\left(\frac{dQ_L'}{dSST'}\right)_{(F-P)} = (\bar{\rho}_a \bar{\Lambda}_v \bar{C}_e)_{(P)} \left[\bar{U}_{10(F)} \left(\frac{dq_s'}{dSST'}\right)_{(F)} - \bar{U}_{10(P)} \left(\frac{dq_s'}{dSST'}\right)_{(P)} \right] \tag{6}$$

Where 'F' represents future values and 'P' represents historical values in the past. As the large-scale wind, $\bar{U}_{10(F)}$ and $\bar{U}_{10(C)}$, experience minimal changes (ranging between -0.4% and -3.5% as shown in Fig. 2)

in the WBCs, Eq. (6) can be further simplified as:

$$\left(\frac{dQ_L'}{dSST'}\right)_{(F-P)} = (\bar{\rho}_a \bar{\Lambda}_v \bar{C}_e)_{(P)} \cdot \bar{U}_{10(P)} \left[\left(\frac{dq_s'}{dSST'}\right)_{(F)} - \left(\frac{dq_s'}{dSST'}\right)_{(P)} \right] \tag{7}$$

Applying a Taylor expansion, the right-hand side term can be approximated as:

$$\left(\frac{dq_s'}{dSST'}\right)_{(F)} - \left(\frac{dq_s'}{dSST'}\right)_{(P)} = \frac{d^2 q_s(T)}{dT^2}\Big|_{T = \overline{SST}_{(P)}} \cdot \Delta SST \tag{8}$$

Substituting (8) into (7) yields:

$$\left(\frac{dQ_L'}{dSST'}\right)_{(F-P)} = (\bar{\rho}_a \bar{\Lambda}_v \bar{C}_e)_{(P)} \cdot \bar{U}_{10(P)} \frac{d^2 q_s(T)}{dT^2}\Big|_{T = \overline{SST}_{(P)}} \cdot \Delta SST \tag{9}$$

Where $\frac{d^2 q_s(T)}{dT^2}$ is determined by C-C scaling and exhibits an exponential increase with temperature. Note that the composite coefficient $(\bar{\rho}_a \bar{\Lambda}_v \bar{C}_e)$ is retained to align the estimated coupling strength changes with magnitude analogous to the actual projections.

Data availability

CMEMS data can be obtained through https://data.marine.copernicus.eu/products. NOAA-OISST can be accessed through https://www.ncei.noaa.gov/products/optimum-interpolation-sst. J-OFURO3 can be achieved through https://www.j-ofuro.com/en/. ERA5 reanalysis can be downloaded from https://doi.org/10.24381/cds.bd0915c6[33]. The CESM simulations can be achieved through https://ihesp.github.io/archive/products/ds_archive/Sunway_Runs.html. The HighResMIP data can be downloaded from https://pcmdi.llnl.gov/CMIP6/. Source data are provided with this paper.

Code availability

MATLAB codes to reproduce the analyses are available upon request from the corresponding author or can be accessed through the link https://zenodo.org/records/10610386.

References

1. Chelton, D. B., Schlax, M. G., Freilich, M. H. & Milliff, R. F. Satellite Measurements Reveal Persistent Small-Scale Features in Ocean Winds. *Science* **414**, 978–983 (2004).
2. Small, R. J. et al. Air–sea interaction over ocean fronts and eddies. *Dyn. Atmospheres Oceans* **45**, 274–319 (2008).
3. Bryan, F. O. et al. Frontal Scale Air–Sea Interaction in High-Resolution Coupled Climate Models. *J. Clim.* **23**, 6277–6291 (2010).
4. Czaja, A., Frankignoul, C., Minobe, S. & Vannière, B. Simulating the Midlatitude Atmospheric Circulation: What Might We Gain From High-Resolution Modeling of Air-Sea Interactions? *Curr. Clim. Change Rep.* **5**, 390–406 (2019).
5. Seo, H. et al. Ocean Mesoscale and Frontal-Scale Ocean–Atmosphere Interactions and Influence on Large-Scale Climate: A Review. *J. Clim.* **36**, 1981–2013 (2023).
6. Xie, S.-P. Satellite Observations of Cool Ocean–Atmosphere Interaction. *Bull. Am. Meteorol. Soc.* **85**, 195–208 (2004).
7. Skyllingstad, E. D., Vickers, D., Mahrt, L. & Samelson, R. Effects of mesoscale sea-surface temperature fronts on the marine atmospheric boundary layer. *Bound.-Layer. Meteorol.* **123**, 219–237 (2007).
8. Chelton, D. B., Schlax, M. G. & Samelson, R. M. Global observations of nonlinear mesoscale eddies. *Prog. Oceanogr.* **91**, 167–216 (2011).
9. Frenger, I., Gruber, N. & Knutti, R. & Münnich, M. Imprint of Southern Ocean eddies on winds, clouds and rainfall. *Nat. Geosci.* **6**, 608–612 (2013).
10. Souza, J. M. A. C., Chapron, B. & Autret, E. The surface thermal signature and air–sea coupling over the Agulhas rings propagating in the South Atlantic Ocean interior. *Ocean Sci.* **10**, 633–644 (2014).

11. Ma, X. et al. Western boundary currents regulated by interaction between ocean eddies and the atmosphere. *Nature* **535**, 533–537 (2016).

12. Ma, X. et al. Importance of Resolving Kuroshio Front and Eddy Influence in Simulating the North Pacific Storm Track. *J. Clim.* **30**, 1861–1880 (2017).

13. Foussard, A., Lapeyre, G. & Plougonven, R. Storm Track Response to Oceanic Eddies in Idealized Atmospheric Simulations. *J. Clim.* **32**, 445–463 (2019).

14. Renault, L., Masson, S., Oerder, V., Jullien, S. & Colas, F. Disentangling the Mesoscale Ocean-Atmosphere Interactions. *J. Geophys. Res.: Oceans* **124**, 2164–2178 (2019).

15. Gan, B. et al. North Atlantic subtropical mode water formation controlled by Gulf Stream fronts. *Natl Sci. Rev.* **10**, nwad133 (2023).

16. Parfitt, R., Czaja, A., Minobe, S. & Kuwano-Yoshida, A. The atmospheric frontal response to SST perturbations in the Gulf Stream region. *Geophys. Res. Lett.* **43**, 2299–2306 (2016).

17. Chen, L., Jia, Y. & Liu, Q. Oceanic eddy-driven atmospheric secondary circulation in the winter Kuroshio Extension region. *J. Oceanogr.* **73**, 295–307 (2017).

18. Sheldon, L. et al. A 'warm path' for Gulf Stream–troposphere interactions. *Tellus A: Dyn. Meteorol. Oceanogr.* **69**, 1299397 (2017).

19. Jiang, Y., Zhang, S., Xie, S.-P., Chen, Y. & Liu, H. Effects of a Cold Ocean Eddy on Local Atmospheric Boundary Layer Near the Kuroshio Extension: In Situ Observations and Model Experiments. *J. Geophys. Res.: Atmos.* **124**, 5779–5790 (2019).

20. Xingzhi, Z., Ma, X. & Wu, L. Effect of Mesoscale Oceanic Eddies on Extratropical Cyclogenesis: A Tracking Approach. *J. Geophys. Res.: Atmos.* **124**, 6411–6422 (2019).

21. Liu, X. et al. Ocean fronts and eddies force atmospheric rivers and heavy precipitation in western North America. *Nat. Commun.* **12**, 1268 (2021).

22. Jing, Z. et al. Maintenance of mid-latitude oceanic fronts by mesoscale eddies. *Sci. Adv.* **6**, eaba7880 (2020).

23. Martínez-Moreno, J. et al. Global changes in oceanic mesoscale currents over the satellite altimetry record. *Nat. Clim. Chang.* **11**, 397–403 (2021).

24. Beech, N. et al. Long-term evolution of ocean eddy activity in a warming world. *Nat. Clim. Chang.* **12**, 910–917 (2022).

25. Ma, X. et al. Distant Influence of Kuroshio Eddies on North Pacific Weather Patterns? *Sci. Rep.* **5**, 17785 (2015).

26. Large, W. & Yeager, S. Diurnal to Decadal Global Forcing for Ocean and Sea-Ice Models: The Data Sets and Flux Climatologies. *NCAR Technical Note* **NCAR/TN-460+STR**, https://doi.org/10.5065/D6KK98Q6 (2004).

27. Yang, P., Jing, Z. & Wu, L. An Assessment of Representation of Oceanic Mesoscale Eddy-Atmosphere Interaction in the Current Generation of General Circulation Models and Reanalyses. *Geophys. Res. Lett.* **45**, 11,856–11,865 (2018).

28. Yuan, M., Li, F., Ma, X. & Yang, P. Spatio-temporal variability of surface turbulent heat flux feedback for mesoscale sea surface temperature anomaly in the global ocean. *Front. Mar. Sci.* **9**, 957796 (2022).

29. Parfitt, R. & Seo, H. A New Framework for Near-Surface Wind Convergence Over the Kuroshio Extension and Gulf Stream in Wintertime: The Role of Atmospheric Fronts. *Geophys. Res. Lett.* **45**, 9909–9918 (2018).

30. Moreton, S., Ferreira, D., Roberts, M. & Hewitt, H. Air-Sea Turbulent Heat Flux Feedback Over Mesoscale Eddies. *Geophys. Res. Lett.* **48**, e2021GL095407 (2021).

31. Hausmann, U., Czaja, A. & Marshall, J. Mechanisms controlling the SST air-sea heat flux feedback and its dependence on spatial scale. *Clim. Dyn.* **48**, 1297–1307 (2017).

32. Chang, P. et al. An Unprecedented Set of High-Resolution Earth System Simulations for Understanding Multiscale Interactions in Climate Variability and Change. *J. Adv. Model. Earth Syst.* **12**, e2020MS002298 (2020).

33. Hersbach, H. et al. The ERA5 global reanalysis. *Q. J. R. Meteorol. Soc.* **146**, 1999–2049 (2020).

34. Faghmous, J. H., Le, M., Uluyol, M., Kumar, V. & Chatterjee, S. A Parameter-Free Spatio-Temporal Pattern Mining Model to Catalog Global Ocean Dynamics. In *2013 IEEE 13th International Conference on Data Mining* 151–160 (2013).

35. Qu, Y., Wang, S., Jing, Z., Wang, H. & Wu, L. Spatial Structure of Vertical Motions and Associated Heat Flux Induced by Mesoscale Eddies in the Upper Kuroshio-Oyashio Extension. *J. Geophys. Res.: Oceans* **127**, e2022JC018781 (2022).

Acknowledgements

Author contributions

X.M. and X.Z conceived the study. X.M. instructed the investigation and wrote the manuscript. X.Z. performed the analyses and produced all figures. L.W. supervised the project. Z.T. contributed to the preprocessing of model data. P.Y., F.S., and M.Y. contributed to the discussion of mesoscale thermal coupling decomposition. Y.Q and H.C. offered insights into eddy detection. Z.J., Z.C., and B.G. contributed to interpreting the results and improving the manuscript.

Competing interests

The authors declare no competing interests.

Additional information

Supplementary information The online version contains supplementary material available at https://doi.org/10.1038/s41467-024-52077-z.

Correspondence and requests for materials should be addressed to Xingzhi Zhang.

Peer review information *Nature Communications* thanks Walter Robinson and the other, anonymous, reviewer for their contribution to the peer review of this work. A peer review file is available.

Reprints and permissions information is available at http://www.nature.com/reprints

Publisher's note Springer Nature remains neutral with regard to jurisdictional claims in published maps and institutional affiliations.